nature communications

Article

https://doi.org/10.1038/s41467-025-63980-4

Self-powered near-infrared mechanoluminescence through MgO/MgF_2 piezo-photonic heterojunctions

Received: 12 March 2025

Accepted: 3 September 2025

Published online: 07 October 2025

Check for updates

Sheng Wu[1,3], Shunyu Wang[1,3], Zhigang Shao[1], Yinzhen Wang[1] & Puxian Xiong[2,3]

Near-infrared mechanoluminescent (NIR ML) materials attract considerable attention for their force-to-light conversion capabilities. However, current materials generally have disadvantages such as high threshold and poor self-recovery ability, which limit their practical applications. Herein, we present a self-powered NIR ML material MgF_2:Cr^{3+}, which does not require pre-charging process. Leveraging the structural similarity between MgF_2 and MgO, we design a MgO/MgF_2:Cr^{3+} heterojunction piezo-photonic system that exhibits high intensity, low activation threshold, and excellent self-powered ML performance. By tuning the molar ratio of MgO to MgF_2, the optimized ML intensity enhances by ≈18 times. Kelvin probe force microscopy surface potential measurement reveals a significant built-in electric field at MgF_2:Cr^{3+} heterojunction interface. Based on the first-principle calculation results, the excellent ML performance originates from the offset of the valence band and the conduction band in the MgO/MgF_2:Cr^{3+} heterostructure and the narrowing of the band gap, which significantly improve the electron ($4.09 \times 10^2\,cm^2\,V^{-1}\,s^{-1}$) and hole ($4.62 \times 10^2\,cm^2\,V^{-1}\,s^{-1}$) mobility, thereby boosting charge transfer and recombination processes. This study provides a strategy for designing high-performance self-powered NIR ML materials based on interfacial effects, offering insights into their expanded applications in the potential bio stress related biological field.

Mechanoluminescent (ML) materials, as an emerging light source converter, exhibit force to light conversion characteristics. Compared with electroluminescence, persistent luminescence (PersL), etc., ML can be driven by mechanical energy (such as friction, tension, compression and impact forces), ubiquitous in nature to achieve sustained and stable light emission[1–6]. Due to its non-contact nature, stress visualization and excellent biological tissue penetration ability. Sensing technology based on near-infrared (NIR) ML has shown broad application prospects in non-destructive testing[7–9], structural health monitoring[10,11], in situ imaging in vitro[12,13], and optogenetic[14,15] research.

Although Cr^{3+} ions exhibit broad application potential in the field of luminescent materials, research on Cr^{3+}-based ML started relatively late. In 2014, the early report on the destructive ML of Cr^{3+}-doped alumina revealed its potential as a mechanical energy-to-light converter[16]. Later, in 2019, we aimed to propose Cr^{3+}-based elastic NIR ML materials and made some preliminary progress in this field[17]. However, research progress on Cr^{3+}-doped NIR-ML materials has

[1]Guangdong Basic Research Center of Excellence for Structure and Fundamental Interactions of Matter, Guangdong Provincial Key Laboratory of Quantum Engineering and Quantum Materials, School of Physics, South China Normal University, Guangzhou, China. [2]Department of Electrical and Electronic Engineering, The University of Hong Kong, Hong Kong, China. [3]These authors contributed equally: Sheng Wu, Shunyu Wang, Puxian Xiong.
e-mail: pxxiong@hku.hk

remained slow over the past decade[3,7,9,10,17–29]. Unfortunately, most current NIR-ML materials rely on defect induction and have problems of non-self-recovery ability, which severely limits their potential applications in the biological field. In addition, the pre-charging process is often accompanied by the generation of PersL signals, further reducing the stability of the ML signal. Importantly, in bioimaging applications, fluctuations in ambient temperature can significantly aggravate the interference of PersL signals and reduce the resolution of NIR-ML materials in real-time high-precision bioimaging. To address these challenges, we previously proposed a chemical co-substitution strategy, introducing both "shallow" and "deep" defects simultaneously into the energy gap to distinguish the emission pathways of PersL and ML signals[9]. This captures the ML signal from the "noise background" generated by PersL. However, this approach sacrifices some charge carriers, leading to a significant reduction in ML intensity. Therefore, overcoming the limitations of defect control and developing self-powered NIR-ML materials capable of maintaining stable force-to-light responses under complex environmental conditions will be the key pathway to overcoming this bottleneck.

To date, researches on NIR ML materials have primarily focused on two aspects: the development of more advanced materials and the performance optimizations of existed ones. First, significant progress has been made in overcoming the limitations of traditional ML materials, which are confined to non-centrosymmetric crystal structures. By adopting centrosymmetric crystal structures, highly efficient Cr^{3+}-activated NIR emission has been obtained[18,27]. On the other hand, strategies to improve ML material performance include solvent engineering, lattice engineering, and energy-level engineering. In solvent engineering, the introduction of specific solvents accelerates sintering reactions and induces the formation of defects and luminescent centers. For example, the addition of Li_2CO_3 as a flux in ZnS: Mn is significantly increased the sulfur vacancy concentration, promoting non-radiative energy transfer and thereby optimizing the ML performance[30]. In lattice engineering, appropriate doping elements are introduced to modulate the crystal field environment and defect concentration. For instance, substituting Al^{3+} for Ga^{3+} effectively improves the optical and mechanical properties of crystals, significantly boosting ML intensity in 650–1000 nm NIR spectral range, with an enhancement up to 475%[27]. In energy level engineering, Cr^{3+} ions act as electronic bridges to modulate energy levels, enabling energy transfer from Cr^{3+} to Nd^{3+} to "switch on" the NIR ML from Nd^{3+} ion. This aims to further enable ML with NIR-II ML biological window emission[3]. In addition, heterojunction technology has become an important means to optimize material performance in recent years because it can effectively regulate carrier mobility through built-in electric fields (BEFs), thereby significantly improving the optoelectronic properties of materials. For example, Shi et al. reported the kinetic Wulff-shaped heteroepitaxial growth of halide perovskites, achieved the preparation of phase-pure two-dimensional halide perovskite epitaxial heterojunctions, and adjusted the interface lattice mismatch, showing the potential for application in advanced optoelectronic devices[31]. Han Htoon et al. created a monolayer $WSe_2/NiPS_3$ heterostructure under zero external magnetic field by nanoindentation, achieving a chiral quantum light source with high circular polarization and single-photon purity[32]. Lu et al. achieved ferroelectricity accompanied by Coulomb screening in different van der Waals heterostructures without Moiré interfaces, and they observed the ferroelectric hysteresis response in BN/monolayer graphene/BN and BN/WSe_2/monolayer graphene/WSe_2/BN heterostructures, broadening the material and design limitations of sliding ferroelectric device applications[33]. Notably, heterojunction technology has also shown great potential in the field of ML, especially in optimizing the luminescence efficiency of materials[34]. In 2020, a ZnS/CaZnOS heterostructure ML material was reported that exhibited 2.2–3.5 times improvement in ML intensity. Other heterostructures, such as $NaNbO_3/LiNbO_3:Pr^{3+}$ and $ZnO/ZnF_2:Mn^{2+}$, also showed improvements of ML intensity around ≈2.5 and ≈9 times, respectively. However, current research has mainly focused on visible ML materials, and the study of NIR ML heterojunctions remains challenging, particularly achieving a significant increase in ML intensity (Table 1).

Table1 | Current advances in ML materials based on heterojunction technology

Materials	Spectral range	ML intensity enhancement	Ref.
ZnS/CaZnOS: Mn^{2+}	500–700 nm	2.2–3.5	49
CaZnOS/ZnS/SrZnOS: Mn^{2+}	500–700 nm	60	60
ZnS/SrZnOS: Mn^{2+}	500–700 nm	≈16	61
ZnO/ZnS: Mn^{2+}	500–700 nm	≈7	62
ZnO/MgF_2: Mn^{2+}	500–700 nm	≈6	62
ZnO/ZnF_2:Mn^{2+}	500–700 nm	≈9	62
ZnO/CaZnOS: Mn^{2+}	500–700 nm	≈2–3	62
$(Ca_{0.5}Sr_{0.5})$ZnOS/ZnS/Mn^{2+}	500–700 nm	≈2.8	63
$NaNbO_3/LiNbO_3:Pr^{3+}$	450–950 nm	≈2.5	64
$Na_{0.8}Mg_{0.2}NbO_3$:0.01Pr^{3+}	580–660 nm	≈2.3	50
MgO/MgF_2:Cr^{3+}	600–1000 nm	≈18	This work

In this study, we report a self-powered NIR ML material MgF_2: Cr^{3+}, which does not rely on high energy beam pre-irradiation such as ultraviolet pre-charging. Even after multiple repeated tests at 473 K, the ML intensity remains at stable level. Importantly, by introducing MgO in different molar ratios, we fabricated a series of MgO/MgF_2: Cr^{3+} binary heterostructure materials. Experimental results show that under small load (≈1 N), the MgO/MgF_2 heterostructure exhibits significant and repeatable NIR ML signals in 700–1000 nm spectral range, with the maximum ML intensity being ≈18 times higher than that of MgF_2: Cr^{3+}. Atomic force microscopy measurements further confirmed the crucial role of the heterostructure in enhancing the piezoelectric properties of the ML material. Furthermore, additional experimental characterization and theoretical calculations validated the formation of the heterojunction. Scanning electron microscopy (SEM) and high-resolution transmission electron microscopy (TEM) were used to conduct detailed structural analysis of the heterojunction, revealing the interfacial characteristics between MgO and MgF_2. Kelvin probe force microscopy (KPFM) tests showed a distinct difference in work function between the interface and other regions of the MgO/MgF_2 combinations, indicating the presence of an internal electric field within the heterojunction, leading to a potential discontinuity. X-ray photoelectron spectroscopy (XPS) analysis further confirmed the formation of the MgO/MgF_2 heterojunction, with notable shifts in the binding energies of the Mg 1*s*, Mg 2*p*, O 1*s*, and F 1*s* peaks, revealing chemical state changes and charge transfer phenomena at the interface, thereby validating the successful construction of the heterojunction. Finally, the significant improvement in electron ($1.07 \times 10^2 \rightarrow 4.09 \times 10^2\ cm^2\ V^{-1}\ s^{-1}$) and hole ($1.72 \times 10^2 \rightarrow 4.62 \times 10^2\ cm^2\ V^{-1}\ s^{-1}$) mobility provided insights into the intrinsic mechanism of ML performance enhancement in heterostructures. This study offers perspectives for the design and development of efficient self-powered NIR ML materials and demonstrates the significant potential of heterojunction technology in optimizing material performance.

Results

Structural and photoluminescent properties of MgF_2:Cr^{3+}

Figure 1 shows the structural and luminescent properties of MgF_2: Cr^{3+} materials with different concentrations. MgF_2 crystal belongs to the tetragonal crystal system, with a space group of $P4_2/mnm$ and a typical zircon-type structure. The magnesium ions (Mg^{2+}) form nearly octahedral coordination with six fluoride ions (F^-), while the fluoride ions

https://doi.org/10.1038/s41467-025-63980-4

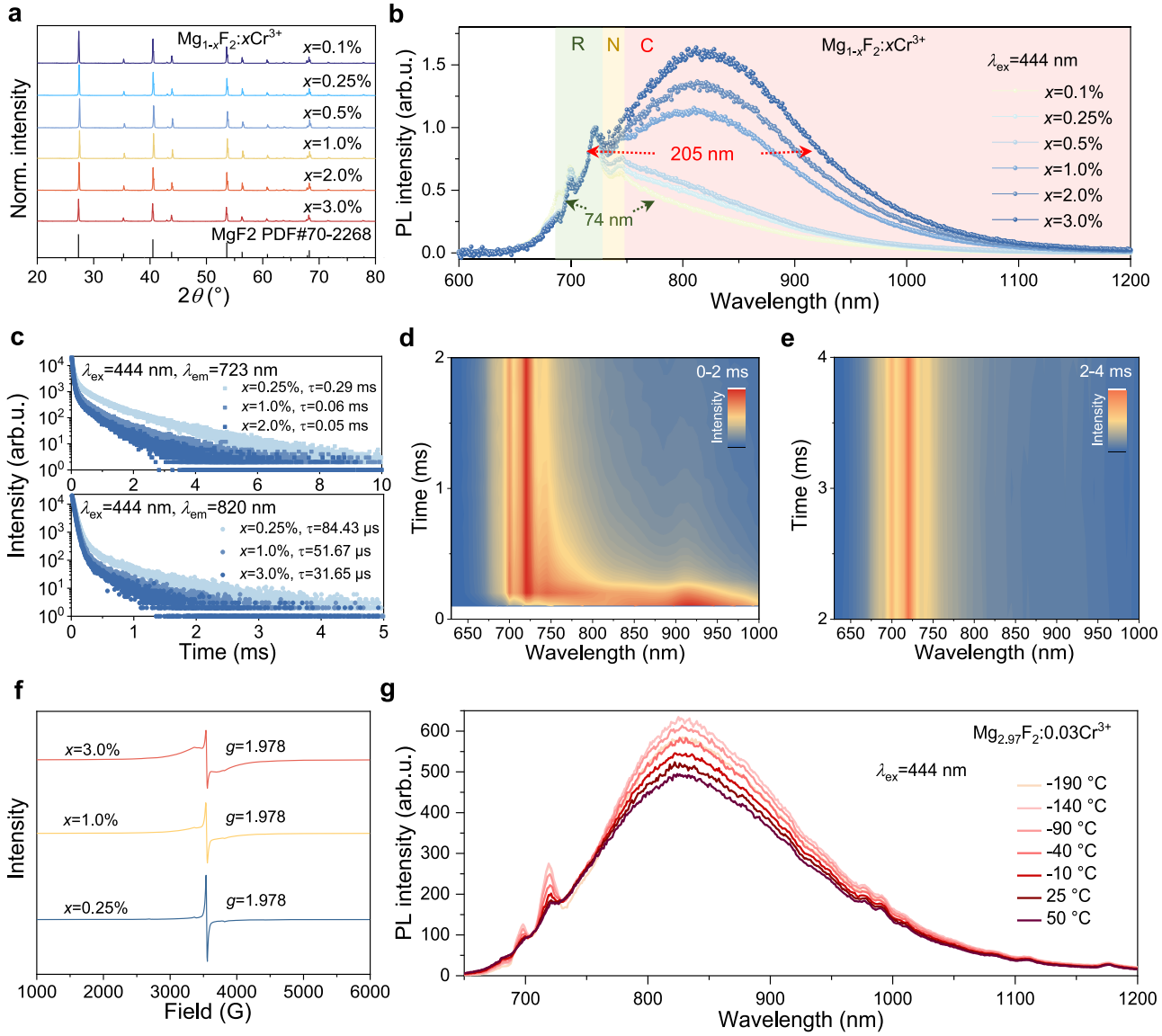

Fig. 1 | Phase structure and PL properties of $Mg_{1-x}F_2$:xCr^{3+}. **a** XRD patterns of $Mg_{1-x}F_2$:xCr^{3+} (x = 0.1–3.0%). **b** PL emission spectra of $Mg_{1-x}F_2$:xCr^{3+} (x = 0.1–3.0%) under 444 nm excitation, with characteristic Cr^{3+} emissions in R-band (≈700 nm), N-band (≈750 nm) and C-band (>800 nm). **c** Luminescence decay profiles peaked at 723 nm (top) and 820 nm (bottom) for samples of x = 0.25, 1.0, and 3.0 under 444 nm excitation. Time-resolved PL maps of $Mg_{2.97}F_2$:0.03Cr^{3+} under 444 nm excitation within **d** 0–2 ms and **e** 2–4 ms, showing dynamic emission evolution over time in the NIR region. The color scale represents intensity on a linear scale. **f** EPR patterns of $Mg_{1-x}F_2$:xCr^{3+} (x = 0.25%, 1.0%, and 3.0%). **g** Temperature-dependent PL spectra of $Mg_{2.97}F_2$:0.03Cr^{3+} under 444 nm excitation from −190 °C to 50 °C. Source data are provided as a Source Data file.

are bridged between multiple magnesium ions, creating a highly symmetric and mechanically stable lattice (Supplementary Fig. 1a)[35,36]. By introducing transition metal ions, the luminescent properties of MgF_2 can be precisely tuned, particularly for optimizing the ML response. Specifically, the X-ray diffraction (XRD) patterns of $Mg_{1-x}F_2$:xCr^{3+} (x = 0.1–3.0%) match well with the reference PDF#70-2268 (Fig. 1a). Furthermore, the Rietveld refinement of the XRD data yielded an excellent reliability factor, further confirming the phase purity of the samples (Supplementary Fig. 1b).

Under 442 nm excitation, the photoluminescence (PL) spectra of $Mg_{1-x}F_2$:xCr^{3+} (x = 0.1–3.0%). exhibits a complex profile with at least three distinct emission components of the R, N, and C band emissions (Fig. 1b, Supplementary Fig. 1c)[37]. The first emission component (R) consists of two strong R-lines at ≈699 nm and 722 nm, corresponding to the $^2E \rightarrow {}^4A_2$ transition, with narrow-line structures caused by phonon-assisted transitions observed near these R-lines. The second emission component (N) appears as a narrow band at 746 nm, and its intensity increases with increasing Cr^{3+} content (x), typically being classified as the N line or N band ($^2E \rightarrow {}^4A_2$ transition). The third emission component (C) is observed in the broad range of 750–1200 nm, whose intensity also increases with Cr^{3+} content. When x > 0.5%, the C band emission becomes dominant in the entire PL spectra. To investigate the emission mechanism of MgF_2:Cr^{3+} in the 750–1200 nm spectral range, we ruled out the possibility that Cr^{3+} occupies different lattice sites with $^4T_2 \rightarrow {}^4A_2$ transition. Since the MgF_2 crystal contains only one kind of Mg lattice site. On the other hand, to reveal the broadband NIR emission mechanism, we monitored the luminescence decay curves at 723 and 820 nm (Fig. 1e). Among them, the emission lifetime at 723 nm is in the millisecond range, representing the typical characteristics of the long-lived $^2E \rightarrow {}^4A_2$ transition of Cr^{3+}. With the increase of Cr^{3+} concentration, the emission lifetime gradually decreases, which is mainly attributed to the concentration quenching effect. At the same time, the emission at 913 nm has a

microsecond lifetime, which is a characteristic of the $^4T_2 \rightarrow {}^4A_2$ spin-allowed transition of Cr^{3+}. According to the calculations based on Eqs. (1)–(3),

$$Dq = \frac{E(^4T_2 - {}^4A_2)}{10} \quad (1)$$

$$\triangle E = E(^4A_2 \rightarrow {}^4T_1) - E(^4A_2 \rightarrow {}^4T_2) \quad (2)$$

$$\frac{Dq}{B} = \frac{15(\frac{\triangle E}{Dq} - 8)}{(\frac{\triangle E}{Dq})^2 - 10\frac{\triangle E}{Dq}} \quad (3)$$

where E ($^4T_1$) and E ($^4T_2$) are the energy positions of $^4T_1$ and $^4T_2$, respectively. The relationship between Stokes shift and bandwidth was also considered, and E was determined as the average of the peak energies of the $^4A_2 \rightarrow {}^4T_2$ excitation band and $^4T_2 \rightarrow {}^4A_2$ emission band. Note: Dq/B represents the crystal field strength. The crystal field strength of Cr^{3+} in an octahedral coordination environment tends to stabilize at higher concentrations, indicating that its influence on the crystal field parameters within the electronic structure gradually diminishes (Supplementary Fig. 1d–f, Supplementary Table 1). Considering the significantly reduced interionic distance between Cr^{3+} ions under high-concentration conditions, the observed PL broadband emission may originate from interactions between Cr^{3+}-Cr^{3+} pairs. In addition, time-resolved photoluminescence (TRPL) spectra were collected under 444 nm excitation over a time range of 0–4 ms (Fig. 1c–e). Specifically, Fig. 1d displays the emission behavior within the initial 0–2 ms, capturing the fast decay dynamics at the early stage of excitation. In contrast, Fig. 1e highlights the delayed emission occurring between 2 and 4 ms, which reveals the presence of long-lived emissive components. The different time windows are complementary and together provide a complete depiction of the photoluminescence dynamics mechanism. As the acquisition time increases, the ^2E energy level emission near 700 nm gradually dominates, while the broadband emission (800–1000 nm) decays rapidly[38]. Among them, the characteristics of the emission spectrum changed with time, emphasizing the inequivalence of different luminescence centers having different decay time. To explore the $^4T_2 \rightarrow {}^4A_2$ transition that occurs in a strong crystal field, we performed electron paramagnetic resonance (EPR) spectroscopy measurements on $Mg_{1-x}F_2{:}xCr^{3+}$ (x = 0.25%, 1.0%, 3.0%) (Fig. 1f). The strong magnetic field signal observed at $g \approx 1.978$ indicates the existence of exchange coupling between Cr^{3+}-Cr^{3+} ion pairs. With the increase of Cr^{3+} concentration[39,40], the intensity of the high magnetic field signal increases, indicating that the concentration of Cr^{3+}-Cr^{3+} ion pairs is high in the heavily doped samples. Furthermore, with the increase of Cr^{3+} concentration, the local environment of the Cr^{3+}-Cr^{3+} ion pairs is distorted, resulting in enhanced interactions between adjacent Cr^{3+} ions, which in turn leads to a significant broadening of the high magnetic field signal. It is worth noting that no resonance signal was observed in the low magnetic field range ($g \approx 4.97$), indicating that Cr^{3+} ions mainly exist in the form of Cr^{3+}-Cr^{3+} ion pairs, and there are no isolated Cr^{3+} ions. In addition, at different temperatures, we observed that the Cr^{3+} emission peak in the 650–750 nm region almost completely disappeared with increasing temperature, while the emission intensity in the 750–1200 nm band changed more gently and always dominated the luminescence (Fig. 1g, Supplementary Fig. 2). Based on these results, we preliminarily attributed the broadband NIR emission to the interaction of Cr^{3+}–Cr^{3+} ion pairs, indicating that the luminescence properties of this material are the result of the combined action of multiple luminescence centers and energy transfer pathways.

Moreover, the efficient broadband NIR emission properties prompted us to further explore the ML characteristics of $Mg_{1-x}F_2{:}xCr^{3+}$ (x = 0.1–3.0%). Excitedly, without any pre-charging process, a significant NIR broadband emission in the 650–1000 nm range was observed upon applying just a 10 N load (Supplementary Fig. 3a). This phenomenon indicates that $MgF_2{:}Cr^{3+}$ has optical response under mechanical stimulation, particularly in its self-powered NIR ML broadband emission. Importantly, a strong linear relationship was observed between the ML intensity and applied load (Supplementary Fig. 3b, c), and after thermal treatment at 473 K and ten consecutive load cycles, the ML intensity was not obviously decreased (Supplementary Fig. 3d, e), demonstrating the material's ML stability and reproducibility. In addition, further thermoluminescence (TL) measurements were conducted to assess the trap states of $Mg_{1-x}F_2{:}xCr^{3+}$ (x = 0.1–3.0%). After a 2-min 254 nm UV charging, no noticeable TL peaks were observed, indicating that the material does not possess significant trap states (Supplementary Fig. 3f). Additionally, vertical decay measurements of the PersL curve did not reveal any shallow traps associated with PersL, further confirming the self-powered ML characteristics of $MgF_2{:}Cr^{3+}$ (Supplementary Fig. 4). These results suggest that $MgF_2{:}Cr^{3+}$ can generate ML without external irradiation, demonstrating good stability and reproducibility under both high temperature and mechanical load, with broad potential for precise mechanical stress sensing in complex environments.

ML and piezoelectric performance of $MgO/MgF_2{:}Cr^{3+}$

Considering the spin-forbidden transitions of Cr^{3+}, its transition behavior is generally constrained by the crystal field symmetry and selection rules. However, crystal field distortion can effectively break these symmetry constraints, further modulating its luminescent properties, which is known to significantly enhance ML performance[3,17,20,25,26,27]. Based on this, we employed a cation substitution strategy aimed at optimizing the crystal structure of $MgF_2{:}Cr^{3+}$ to increase ML intensity. Specifically, we substituted Li^+ for Mg^{2+} to achieve charge balance through the $Li^+ + Cr^{3+} \leftrightarrow 2Mg^{2+}$ exchange, and partially substituted Ca^{2+} for Mg^{2+} to distort the crystal field, further adjusting the local environment to enhance ML performance. However, although the introduction of Li^+ and Ca^{2+} does not alter the phase structure of the material, the ML intensity of the substituted $MgF_2{:}Cr^{3+}$ samples are significantly decreased, and this is eventually disappeared (Supplementary Fig. 5). Further analysis revealed no formation of additional defect states, indicating that the cation substitution strategy did not effectively improve the ML performance as anticipated.

To further optimize the ML performance of $MgF_2{:}Cr^{3+}$, we constructed heterojunctions with different material interfaces. By precisely tuning the energy band structures and interfacial effects of the heterojunctions, we effectively improved the ML performance. Specifically, we introduced CaO, ZnO and MgO to construct heterojunctions and prepared a series of heterogeneous materials with different molar ratios. The experimental results are promising, as all three types of heterojunctions significantly enhanced the ML intensity (Fig. 2, Supplementary Fig. 6). In particular, the MgO/MgF_2 heterojunction showed a significant effect in enhancing ML performance, further verifying the great potential of heterojunction structure in optimizing ML properties. Additionally, significant changes in the material's appearance and luminescent properties were observed when treated at different temperatures (1000, 1100, 1200, and 1300 °C). As the temperature increased to 1200 °C, the material became more uniform and dense, and its luminescence intensity was significantly enhanced. Between 1000 and 1200 °C, the ML intensity progressively increased, reaching its peak at 1200 °C, indicating that higher heat treatment temperatures help optimize the crystal structure and activate more luminescent centers. The effect of holding time on ML intensity was minimal at 1200 °C, indicating that it contributed little to performance improvement (Supplementary Fig. 7). Therefore, we selected 1200 °C for 1 h as the final synthesis condition for this study.

To quantify the ML performance, the powder samples were molded in low-density polyethylene (LDPE) and sandwiched between two

https://doi.org/10.1038/s41467-025-63980-4

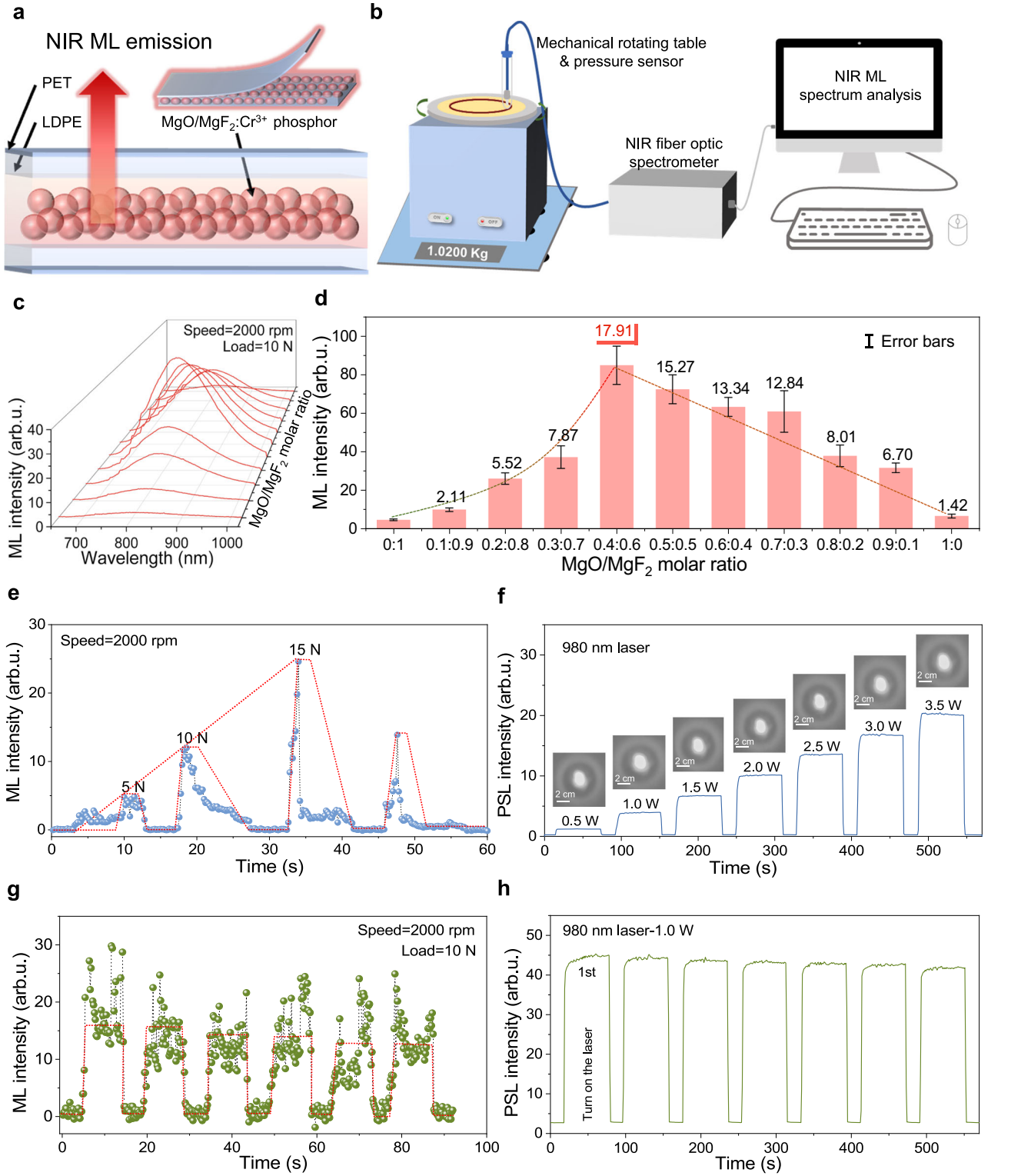

Fig. 2 | ML performance of $MgO/MgF_2:Cr^{3+}$ heterostructures. a Schematic illustration of the flexible composite ML film consisting of PET/LDPE layers embedded with $MgO/MgF_2:Cr^{3+}$ phosphor. **b** Diagram of the custom-built ML measurement setup, comprising a mechanical rotation platform, pressure sensor, and NIR fiber optic spectrometer. **c** ML emission spectra of $MgO/MgF_2:Cr^{3+}$ samples with varying MgO: MgF_2 molar ratios under 10 N load and 2000 rpm rotation speed. **d** Corresponding integrated ML intensities showing a maximum at a MgO: MgF_2 ratio of 0.4:0.6. Error bars represent standard deviations from ten repeated measurements. **e** ML intensity response under variable loads (5–15 N), showing load-dependent emission enhancement. **f** PSL intensity variation under different 980 nm laser powers (0.5–3.5 W), with insets showing corresponding emission spot images. **g** ML intensity profile under cyclic loading, demonstrating ML signal reproducibility and mechanical stability. **h** Repeated PSL response cycles under 1.0 W 980 nm laser excitation, demonstrating stable PSL behavior. Source data are provided as a Source Data file.

polyethylene terephthalate (PET) films, which are tested using a homemade ML test system (Fig. 2a, b). We observed that the ML performance of the MgO/MgF_2: Cr^{3+} heterostructure was strongly influenced by the molar ratio of MgO to MgF_2 (Fig. 2b). Specifically, when the ratio of MgO/MgF_2 was 2:3, the ML intensity of the MgO/MgF_2: Cr^{3+} was ≈18 times higher than that of MgF_2:Cr^{3+} (Fig. 2c, d). Obviously, the different ratios of MgO to MgF_2 may affect the volume of the heterojunction and the thickness of each component, which may be the reason for the variation in ML performance. It is worth noting that as the MgO/MgF_2 molar ratio increases, the ML intensity exhibits exponential increasement up to a 2:3 molar ratio. This is primarily due to the gradual optimization of the heterojunction interface energy levels, which significantly enhances carrier transport and recombination efficiency under bandgap modulation. However, when the MgO/MgF_2 molar ratio exceeds 2:3, the increase in interface non-radiative recombination centers and bandgap mismatch may reduce carrier recombination efficiency, leading to a linear decline in ML intensity. This suggests that carefully tailoring the composition ratio of the heterojunctions between different materials is crucial for effectively controlling their ML performance. Moreover, although the ML intensity of MgO/MgF_2: Cr^{3+} reaches only 42.96% of that of commercial ZnS: Mn^{2+} phosphors under identical loading conditions, its emission in the NIR region endows it with distinct advantages and significant potential for applications in stress sensing and bioimaging (Supplementary Fig. 8).

A deeper understanding of the mechanisms behind self-powered ML materials is of significant research importance for the design of efficient ML materials. Figure 2e displays the typical transient response characteristics of MgO/MgF_2:Cr^{3+} under varying loads: as the load is applied, the ML intensity rapidly increases linearly, followed by a quick decay. This transient behavior indicates that ML generation is highly dependent on the instantaneous excitation induced by mechanical loads, with the energy source likely stemming from stress-induced charge separation and recombination at the interface. Further analysis reveals significant variations in ML intensity under different load conditions, suggesting that it is not only closely related to the activation level of the interface energy states but also directly tied to the charge migration efficiency. Therefore, controlling the excitation of interface energy states and ensuring efficient charge migration are critical factors in enhancing the performance of self-powered ML materials. It is worth noting that the photo-stimulated luminescence (PSL) experiment further verified the photo-responsive characteristics of the material (Fig. 2f). As the laser power increases, the PSL intensity of MgO/MgF_2:Cr^{3+} is significantly increased, indicating that the PSL process can effectively improve the radiative recombination luminescence efficiency of the material by exciting interface defect states. Further cyclic experiments were conducted to verify the stability of MgO/MgF_2:Cr^{3+} under repeated excitation conditions. Figure 2g illustrates that under periodic mechanical loading, the ML intensity exhibits stable periodic fluctuations, indicating that MgO/MgF_2:Cr^{3+} demonstrates excellent ML repeatability and dynamic stability. Similarly, in the seven-cycle experiment with periodic switching of the 980 nm laser, the PSL intensity remained stable with no significant attenuation (Fig. 2h). These results suggest that MgO/MgF_2:Cr^{3+} not only exhibits mechanical and optical response characteristics, but also shows high controllability and efficiency in the activation and recombination mechanisms of its interface energy states under repeated excitation conditions. In conclusion, the luminescence mechanism of MgO/MgF_2:Cr^{3+} depends on the excitation of interface defect states and the associated charge migration and recombination processes. This study provides a solid experimental foundation for understanding the efficient mechanism of mechanical-to-optical energy conversion in self-powered NIR ML materials.

Figure 3 systematically illustrates the ML properties of MgO/MgF_2:Cr^{3+} under different loading modes and their dependence on mechanical parameters. Figure 3a shows that the ML intensity of MgO/MgF_2:Cr^{3+} is significantly increased as the rotational speed increases from 2000 to 6000 rpm, revealing a positive correlation between ML intensity and rotational speed. Dynamic images further demonstrate the ML behavior of MgO/MgF_2:Cr^{3+} at different rotation speeds from 2000 to 6000 rpm (Fig. 3b, Supplementary Fig. 9, Supplementary Movies 1–5). In addition, Fig. 3c shows the time-load triangle wave of MgO/MgF_2:Cr^{3+} in cylindrical sample under different loading conditions using a compression testing machine, indicating the positive correlation between the ML intensity and the applied load. As the load increases, the ML intensity of MgO/MgF_2:Cr^{3+} was significantly enhanced, with the emission area gradually expanding (Fig. 3d, Supplementary Movie 6). In continuous cyclic loading experiments, the ML intensity of MgO/MgF_2:Cr^{3+} exhibits a synchronized periodic response, further confirming its excellent ML stability and transient response to mechanical stimulation (Fig. 3e). It is noteworthy that under friction and impact, MgO/MgF_2:Cr^{3+} powder exhibits a pronounced ML (Supplementary Fig. 10, Supplementary Movies 7, 8). However, when mixed with polydimethylsiloxane, the ML intensity is significantly weakened or even disappeared both under stretching stress and friction (Supplementary Fig. 11, Supplementary Movies 9, 10). This phenomenon suggests that the previously proposed triboluminescence[41,42] and contact-separation-induced models[43] cannot effectively explain our experimental observations. Therefore, the ML observed in MgO/MgF_2:Cr^{3+} is likely attributed to piezoelectricity effect. Figure 3f presents the piezoelectric response characteristics of MgF_2:Cr^{3+} and MgO/MgF_2:Cr^{3+} materials under varying tip bias conditions (±10 V). The typical "butterfly loop" shape clearly illustrates the piezoelectric performance and interface effects of the materials[7]. For pure MgF_2:Cr^{3+} (black curve), the piezoelectric response symmetrically decreases as the absolute value of the bias increases, forming a standard butterfly curve. This indicates that the piezoelectricity of the material is primarily attributed to the reordering of polarization centers induced by lattice distortion under the electric field. In contrast, for the MgO/MgF_2:Cr^{3+} heterostructure (red curve), the piezoelectric response is significantly enhanced, and the response range is widened, suggesting that the introduction of MgO plays a critical role in enhancing interface polarization effects and stress coupling properties. In addition, MgO/MgF_2:Cr^{3+} exhibits a slight asymmetry between the negative and positive bias responses, which may be attributed to the uneven distribution of interface stresses. Figure 3g shows that the MgO/MgF_2:Cr^{3+} device exhibits a significant piezoelectric effect under an applied load of 5 N (see "Methods", device diagram: Supplementary Fig. 12). Among them, the current response (blue curve) shows stable and obvious periodic pulses, and the voltage response (red curve) shows similar periodic fluctuations[44,45]. This shows that the MgO/MgF_2:Cr^{3+} device can continuously and effectively generate current and voltage under periodic loads. These results verify that the MgO/MgF_2:Cr^{3+} heterostructure material has excellent piezoelectric properties and can achieve efficient force-to-electric conversion under mechanical stimulation, further demonstrating its potential and feasibility in piezoelectric sensitivity, wide voltage response, and piezoelectric applications. In addition, Fig. 3h shows the friction cycle test conducted at a load of 7 N and a rotation speed of 700 rpm using a self-assembled integrated friction and wear test platform (the inset is a schematic diagram of the friction test platform)[46]. The results show that the ML intensity remains at a stable level without a sharp drop. After 1200 ML cycles under a 7 N load, the ML intensity can still be maintained at 52% of the initial value. Figure 3i shows a comparison of the frame counts for ML generation by different ML materials captured by a NIR camera[3,9,18,25–27,47]. The upper section features Cr^{3+}-doped ML materials, which are of the defect-controlled type. These materials exhibit slower changes during ML generation, requiring more frames, indicating a slower ML generation rate. In contrast, the bottom section displays piezoelectric ML materials, which show a distinct rapid transition to generate ML, with

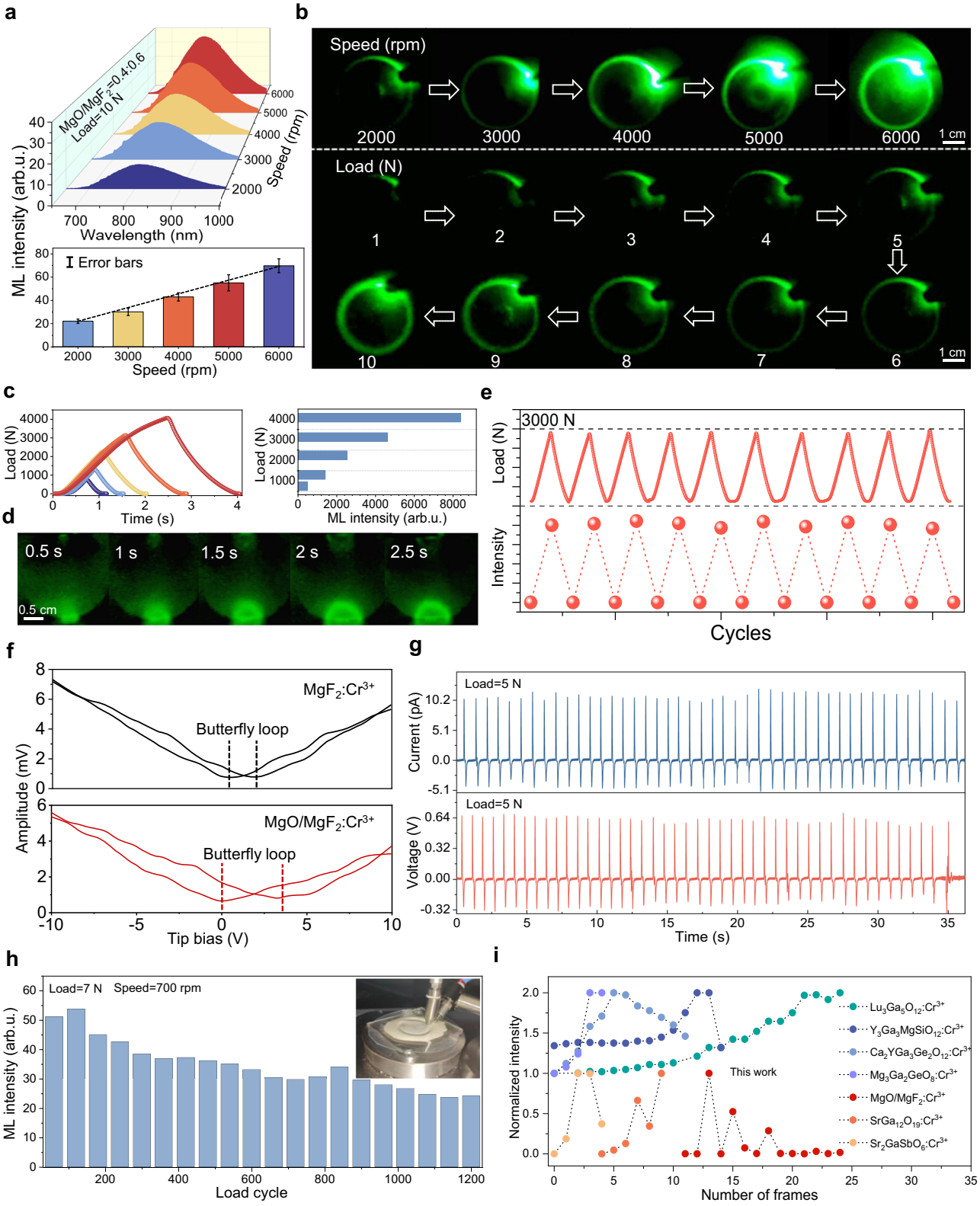

$MgO/MgF_2:Cr^{3+}$ requiring the fewest frames to generate ML. It is noteworthy that piezoelectric ML materials exhibit a faster response and require fewer frames during ML generation, indicating that their ML generation efficiency and rate surpass those of defect-controlled materials. Thus, by comparing the performance of different material types in the ML generation process, the study reveals differences in ML generation rates, providing insights into the luminescent properties and generation speeds of ML materials.

Experimental confirmation of heterostructure formation

The suitability of MgO and MgF_2 for constructing heterostructures is primarily attributed to their high compositional and structural similarity (Supplementary Fig. 13). Both materials are featured with magnesium ions in octahedral coordination, with MgO adopting a regular octahedral geometry, while MgF_2 exhibits a slightly distorted octahedral structure. Moreover, both materials show a high degree of consistency in their local coordination environments, with the chemical

Fig. 3 | Multimodal ML performance and mechanism of MgO/MgF_2:Cr^{3+} heterostructures. a ML emission spectra and corresponding integrated intensities of MgO/MgF_2:Cr^{3+} (MgO: MgF_2 = 0.4:0.6) under different rotation speeds (2000–6000 rpm). Error bars represent standard deviations from ten repeated measurements. **b** Photographs of ML emissions at varying rotation speeds and applied loads, demonstrating bright NIR luminescence under increasing mechanical stimuli. **c** The time-load triangle wave and their corresponding ML intensities under different load. Histogram of ML intensity as a function of load, showing a positive correlation. **d** Time-lapse images of ML response under 10 N load, captured from 0.5 to 2.5 s, showing temporal evolution of ML intensity. **e** ML intensity stability during 10 consecutive cycles under repeated triangular load input, confirming excellent mechanical durability and repeatability. **f** Piezoelectric amplitude–bias curves of MgF_2:Cr^{3+} and MgO/MgF_2:Cr^{3+}, both displaying butterfly-shaped hysteresis loops, indicative of intrinsic piezoelectric behavior. **g** Real-time output current and voltage signals of MgO/MgF_2:Cr^{3+} under 5 N cyclic loading, supporting its self-powered sensing capability. **h** Long-term cyclic ML performance at 700 rpm roation speed and 7 N load, showing consistent emission over >1000 cycles. Inset: Image of the mechanical measurement setup. **i** Comparison of ML generation rates among various NIR ML materials. MgO/MgF_2:Cr^{3+} heterostructure exhibits the quickest ML generation rate, indicating its capability for real-time dynamic sensing and fast-response applications. Source data are provided as a Source Data file.

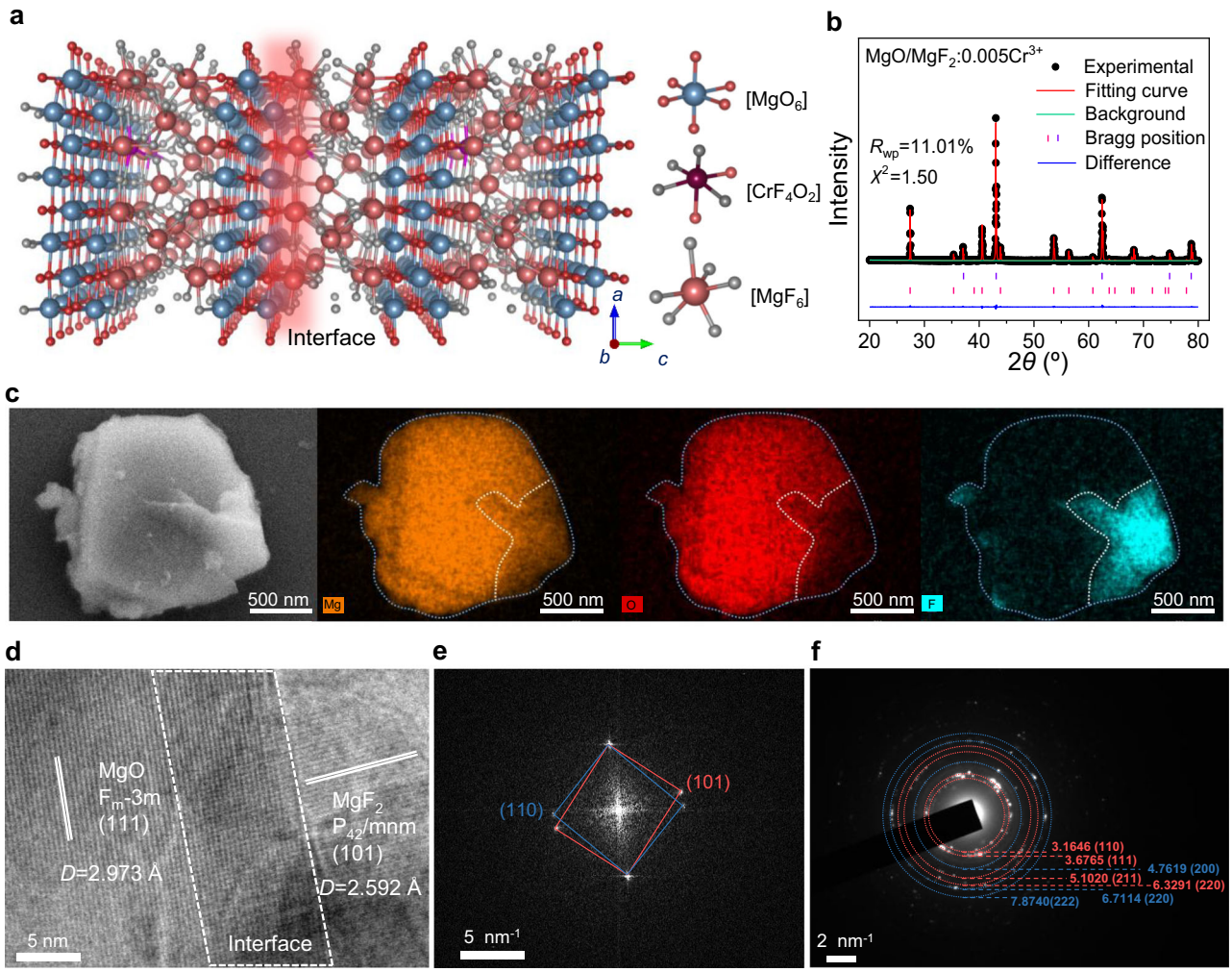

Fig. 4 | Crystal structure and chemical composition of MgO/MgF_2:Cr^{3+} heterostructures. a Schematic illustration of the MgO/MgF_2 interface and local coordination environment of [MgO_6], [CrF_4O_2], and [MgF_6] units. **b** Rietveld refinement of XRD pattern for MgO/MgF_2:0.005Cr^{3+}, confirming the coexistence of MgO and MgF_2 phases with good crystallinity of R_{wp} = 11.01% and χ^2 = 1.50. **c** SEM image and corresponding EDS elemental mapping for Mg, O, and F, showing the spatial distribution and phase separation within a representative heterostructure particle. **d** HRTEM image revealing the well-defined interface between MgO (D = 2.973 Å, (111)) and MgF_2 (D = 2.592 Å, (101)) domains. **e** FFT diffraction pattern from the HRTEM image, with characteristic spots assigned to MgO (110) and MgF_2 (101) planes. **f** SAED pattern of the heterostructure, confirming the coexistence of polycrystalline MgO and MgF_2 phases with indexed diffraction rings corresponding to both components. Source data are provided as a Source Data file.

similarities between oxygen and fluorine ions and the match of their lattice constants. Among them, Fig. 4a clearly shows the specific crystal structure of the MgO/MgF_2 heterojunction. In the MgO region, [Mg^{2+}] is surrounded by six [O^{2-}] to form a typical octahedral structure. Similarly, in MgF_2, [Mg^{2+}] combines with six [F^-] to form a tetrahedral structure centered on [Mg^{2+}]. At the interface of the heterojunction, a transitional coordination structure is formed between [Mg^{2+}], [O^{2-}] and [F^-], resulting in a change in the coordination number and showing transitional state characteristics (Supplementary Fig. 14). The XRD diffraction peaks of MgO/MgF_2:Cr^{3+}, which is perfectly aligned with those of cubic MgO (PDF #65-0476) and orthorhombic MgF_2 (PDF #70-2268) (Supplementary Fig. 15), indicate that both phases coexist in the heterojunction while maintaining their distinct crystalline structures. Combined with the Rietveld refinement analysis, the obtained reliability factor (χ^2 = 1.50, R_{wp} = 11.01%) was within the allowable range, further verifying the successful synthesis of the MgO/MgF_2

https://doi.org/10.1038/s41467-025-63980-4

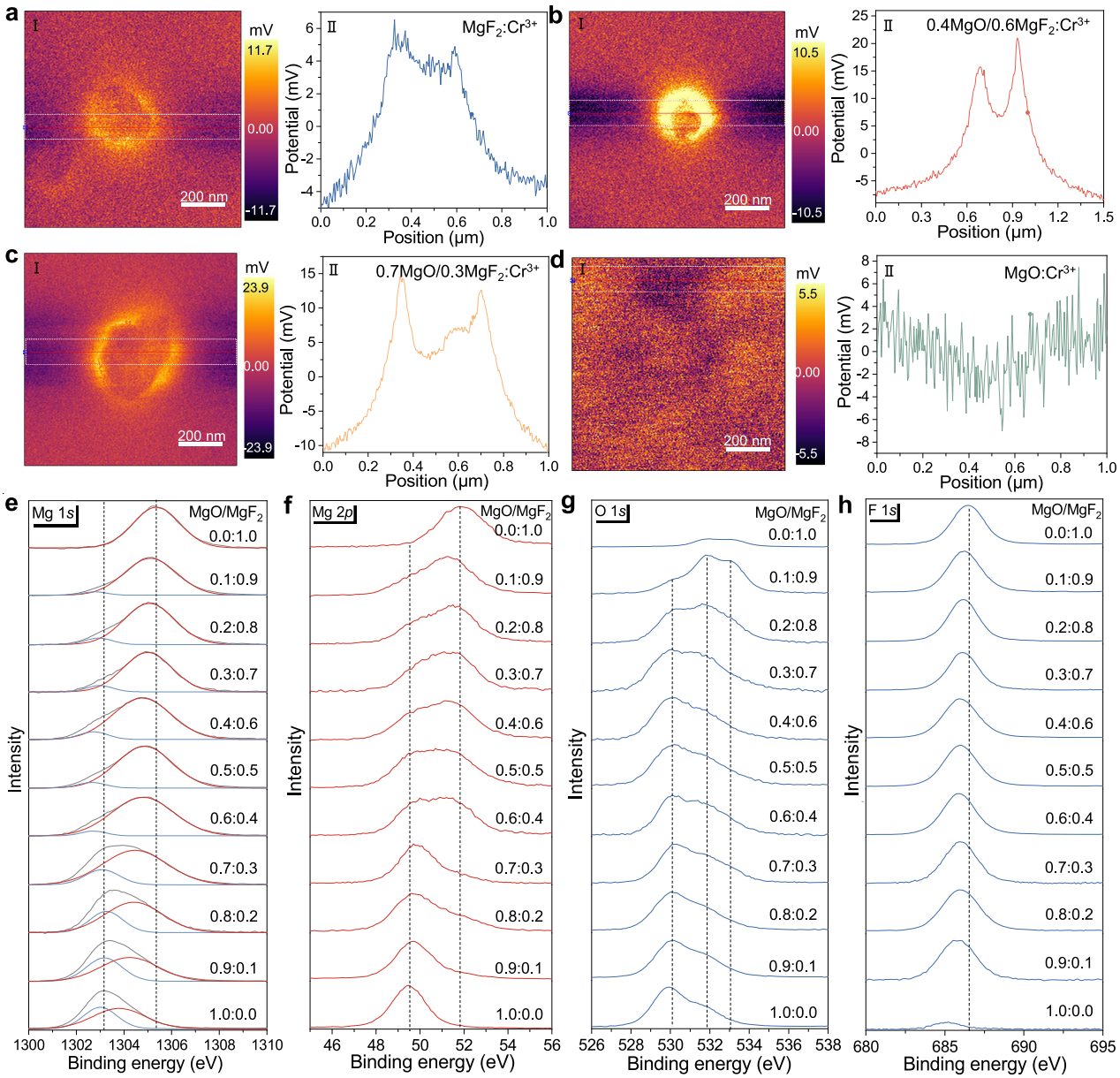

Fig. 5 | Surface potential mapping and chemical state analysis of MgO/MgF_2:Cr^{3+}. a–d Surface potential distribution images (I) and corresponding line profiles (II) for samples measured via KPFM. Samples include MgF_2:Cr^{3+}, 0.4MgO/0.6MgF_2: Cr^{3+}, 0.7MgO/0.3MgF_2: Cr^{3+}, and MgO: Cr^{3+}. High-resolution XPS spectra of Mg 1*s* (**e**), Mg 2*p* (**f**), O 1*s* (**g**), and F 1*s* (**h**) for MgO/MgF_2:Cr^{3+} composites with varying MgO: MgF_2 molar ratios (from 0.0:1.0 to 1.0:0.0). The systematic chemical shifts and peak intensity variations reflect changes in local bonding environments and interfacial composition. Source data are provided as a Source Data file.

heterostructure and the integrity of its crystal structure (Fig. 4b). Additionally, energy-dispersive X-ray spectroscopy (EDS) elemental mapping clearly reveals the geometric and compositional features of the MgO/MgF_2 heterojunction (Fig. 4d). Mg element is uniformly distributed throughout the sample, while O and F elements are concentrated in distinct regions, corresponding to the MgO and MgF_2 phases, respectively, visually confirming the heterojunction formation. In addition, high-resolution transmission electron microscopy (HRTEM) images clearly display the lattice characteristics of both MgO and MgF_2 phases, with the (110) plane of MgO (D = 2.973 Å) and the (101) plane of MgF_2 (D = 2.592 Å) being distinctly observable (Fig. 4e, Supplementary Fig. 16). The well-defined phase boundaries further indicate the stable formation of the heterojunction. Fast fourier transform (FFT) analysis further corroborates the crystallographic features on both sides of the interface, corresponding to the (110) plane of MgO and the (101) plane of MgF_2 (Fig. 4f). Furthermore, the selected area electron diffraction (SAED) patterns further accurately marked the different crystal plane indices of the characteristic diffraction rings of MgO and MgF_2 (Fig. 4g), confirming the crystal structure integrity of the two phases at the microscopic scale and the high-quality heterogeneous combination. Here, the interface layered structure is still clear under different sintering time, and the MgO/MgF_2 heterostructure is always stably formed and is not significantly affected by the holding time (Supplementary Fig. 17).

To precisely measure the surface potential distribution and interfacial electrical properties of MgO/MgF_2 heterostructures, we employed KPFM to measure the surface potential distribution and profile characteristics of different samples (Fig. 5, Supplementary Fig. 18). Among them, we used silicon wafer as the substrate material, its surface shows obvious striped morphology features, while the corresponding surface potential map shows an overall uniform distribution, and no significant potential changes are observed

(Supplementary Fig.19). For the single-phase samples MgF_2: Cr^{3+} and MgO: Cr^{3+} (Fig. 5a, d), the surface potential distribution is uniform, with overall potential values of ≈110 mV and ≈115 mV, respectively, and the profile images show minimal potential fluctuation, indicating the electrical homogeneity of the single-phase materials. In contrast, for the heterostructures 0.4MgO/0.6MgF_2: Cr^{3+} and 0.7MgO/0.3MgF_2: Cr^{3+} (Fig. 5b, c), the potential distribution exhibits distinct regional differences, especially in 0.4MgO/0.6MgF_2: Cr^{3+}, where the central region's potential increases to ≈112 mV, while the edge region shows lower potential. The profile images display a significant potential gradient, suggesting that a BEF may be formed at the MgO/MgF_2 interface, establishing the heterojunction, accompanied by charge transfer or interfacial dipole effects, leading to regional potential variations. Further analysis reveals that the difference in work functions between MgO and MgF_2 at the interface is the key factor driving the potential gradient changes. The work function refers to the minimum energy required for electrons to escape from the material's surface, and it directly influences the electrical properties and interfacial behavior of materials. MgO has a higher surface work function than that in MgF_2. This difference could lead to the formation of an internal electric field at the interface, promoting charge transfer and dipole formation, thereby inducing potential changes. As the MgO content increases (0.4MgO/0.6MgF_2: Cr^{3+} to 0.7MgO/0.3MgF_2: Cr^{3+}), the higher work function of MgO gradually dominates the interfacial potential balance, further weakening the potential contribution from MgF_2, leading to a reduction in the potential gradient and a more uniform potential distribution. These results show that the electrical properties of the MgO/MgF_2 heterostructure are controlled by the phase ratio and work function differences. Optimizing the phase ratio effectively tunes surface potential and electrical properties, with a strong correlation to ML performance trends.

To further validate the chemical origin of the surface potential distribution and interfacial electrical properties measured by KPFM, XPS was employed to systematically analyze the chemical environment and binding energies of the MgO/MgF_2 heterostructure, providing atomic-level insights into the interfacial chemical characteristics and formation mechanisms (Fig. 5e–h). The Mg 1*s* and Mg 2*p* binding energies exhibit distinct double-peak features corresponding to the chemical environments of MgO and MgF_2 (Fig. 5e, f). Specifically, the binding energies of MgO are lower (≈1303.5 eV and ≈49.5 eV), while those of MgF_2 are higher (≈1304.5 eV and ≈50.3 eV). This difference is primarily attributed to the strong electronegativity of F ions, which significantly reduces the electron density around Mg atoms in MgF_2, resulting in an upward shift in their binding energies. Furthermore, as the MgO content increases, the Mg 1*s* and Mg 2*p* binding energies exhibit slight shifts in the interfacial regions, reflecting a transition in the interfacial chemical environment. These binding energy shifts may arise from interfacial charge transfer or dipole effects, providing direct evidence of the interfacial characteristics of the heterostructure. Importantly, the binding energy analysis of O 1*s* and F 1*s* (Fig. 5g, h) further reveals the interfacial chemical properties between the two phases. The O 1*s* binding energy remains stable at ≈530.2 eV, corresponding to the MgO chemical environment, while the F 1*s* binding energy stabilizes at ≈685.0 eV, corresponding to the MgF_2 chemical environment. This indicates that oxygen and fluorine atoms remain confined to their respective phases without significant interphase migration. However, with adjustments in the MgO/MgF_2 molar ratio, the O 1*s* and F 1*s* binding energies show slight shifts in the interfacial region. These shifts further confirm the transitional nature of the interfacial chemical environment, highlighting significant interfacial effects and chemical environment modulation associated with heterojunction formation. These findings elucidate the formation mechanism and interfacial chemical evolution of the MgO/MgF_2 heterostructure, clarifying how phase ratios and work function differences govern charge transfer and dipole effects. This study provides a theoretical foundation for optimizing functional performance and understanding interfacial behaviors in heterostructures.

How does the introduction of heterojunction structure improve ML performance? The physical mechanism behind it is of great research value. To further explore the regulatory effect of heterojunction on the electrical and band properties of materials, we systematically analyzed the Hall effect, ultraviolet photoelectron spectroscopy (UPS) and current-voltage (*I-V*) test results of MgF_2:Cr^{3+} and MgO/MgF^2:Cr^{3+} (Fig. 6a–c, Supplementary Figs. 20, 21). The Hall effect test results show that the MgO/MgF_2:Cr^{3+} heterojunction has a higher carrier concentration ($1.36 \times 10^{15}\,cm^{-3}$) and mobility ($1.76 \times 10^{2}\,cm^2\,V^{-1}\,s^{-1}$), and the resistivity is significantly reduced to $2.61 \times 10^{2}\,\Omega\,cm^{-1}$, indicating that the structure significantly improves the carrier transport capacity. In addition, *I-V* tests further confirmed this: at the same voltage, MgO/MgF_2:Cr^{3+} exhibited a higher current response, reflecting its better conductivity and interfacial electron injection efficiency. Further UPS test results show that the ionization Energy (IE) of MgO/MgF_2:Cr^{3+} is reduced from 16.31 to 16.09 eV, while the valence band maximum (VBM) is increased from 7.10 to 7.32 eV (Bias = −10 V). The reduction in ionization potential means that the energy barrier for electrons to escape from the material is reduced, which is conducive to the generation and migration of excited state electrons. The optimization of the band structure and the synergistic enhancement of carrier behavior jointly promote the excitation efficiency and radiative recombination efficiency of the Cr^{3+} activation center, thereby significantly improving the ML performance of the MgO/MgF_2:Cr^{3+} heterostructure.

First-principles computation and biocompatibility evaluation

To validate the interfacial modulation effects revealed by the experimental results, we further performed first-principles calculations to theoretically analyze the interfacial electronic structure of the MgO/MgF_2:Cr^{3+} heterojunction. To validate the interfacial modulation effects revealed by the experimental results, we further investigated the interfacial electronic structure of the MgO/MgF_2:Cr^{3+} heterojunction via first-principles calculations. Figure 6d presents the charge density difference map of the heterostructure, where the purple and yellow regions indicate electron accumulation and depletion, respectively, revealing a clear charge transfer behavior at the interface. The results indicate that, compared to pristine MgF_2 (Supplementary Fig. 22), the coupling of MgF_2 with MgO leads to a preferential electron transfer from MgF_2 to MgO. This interfacial charge redistribution induces the formation of a BEF at the heterojunction interface, which helps maintain Fermi level equilibrium across the heterostructure. In addition, why can the MgO/MgF_2:Cr^{3+} heterojunction achieve a qualitative leap in ML performance? An important reason may be related to the changes in electronic structure and energy bands. As shown in Fig. 6e, f, the spin-up and spin-down state energy band diagrams of the MgO/MgF_2:Cr^{3+} heterostructure show that there is a clear energy level dislocation at the interface, especially between the spin-up state and the spin-down state[48–50]. In contrast, the spin-polarized energy band structure of MgF_2:Cr^{3+} shows that the energy bands of the spin-up and spin-down states remain relatively separated, and the state density of the spin-down state is relatively concentrated (Supplementary Figs. 23, 24). At the same time, the magnetic moment of the MgO/MgF_2:Cr^{3+} heterostructure is −3.9898 μB, while that of MgF_2:Cr^{3+} is 3.9991 μB, which proves the existence of significant spin polarization effect in the MgO/MgF_2:Cr^{3+} heterostructure and reveals the change of magnetism at the interface. Therefore, the rearrangement of electrons and spins leads to a significant decrease in the band gap of the MgO/MgF_2:Cr^{3+} heterostructure (3.178 eV), providing possibilities for the further application of this material. Another key factor is whether the change in bandgap is related to stress (strain). By calculating the strain response of the material along the y-axis, we observed some

https://doi.org/10.1038/s41467-025-63980-4

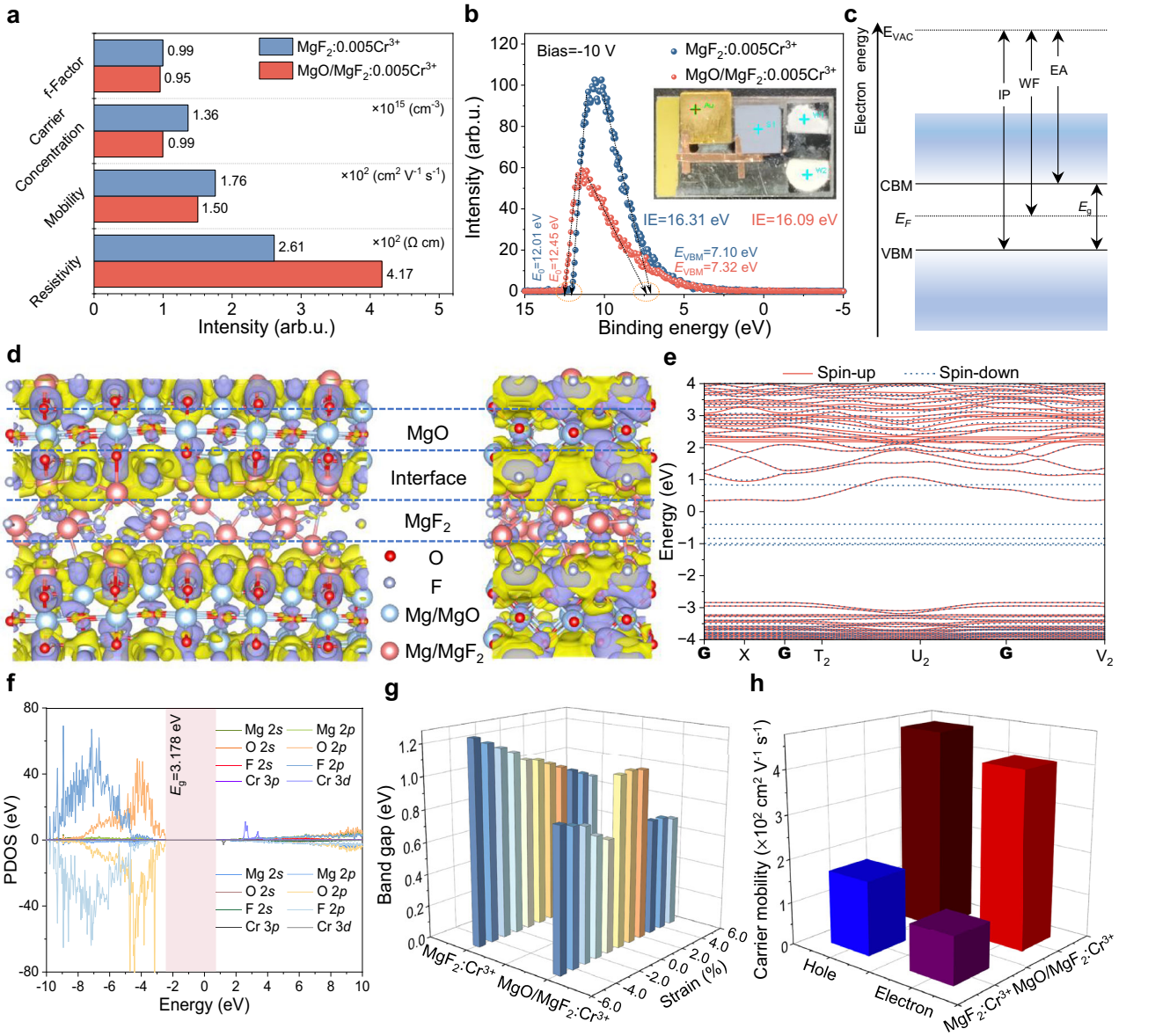

Fig. 6 | Electronic structure properties of MgO/MgF_2:Cr^{3+} obtained by first-principles calculations. a Hall effect measurement comparing key electrical properties of MgF_2:0.005Cr^{3+} and MgO/MgF_2:0.005Cr^{3+}, including the F-factor, carrier concentration, carrier mobility, and resistivity; **b** UPS spectra of MgF_2:0.005Cr^{3+} and MgO/MgF_2:0.005Cr^{3+}, with the extracted IE and VBM indicated. The inset shows the actual UPS measurement setup. **c** Schematic illustration of the electronic band structure, highlighting the definitions and relative positions of the IE, work function (WF), and electron affinity (EA). **d** Front and side views of the charge density difference of MgO/MgF_2:Cr^{3+}. The purple and yellow areas represent electron depletion and accumulation, respectively. **e** Energy band diagram of MgO/MgF_2:Cr^{3+}. **f** Density of states distribution of MgO/MgF_2:Cr^{3+}. **g** Comparison of the band gap of MgF_2:Cr^{3+} and MgO/MgF_2:Cr^{3+} as the strain increases from −5% to 5% along the *y*-axis. **h** Electron/hole mobility of MgF_2:Cr^{3+} and MgO/MgF_2:Cr^{3+}. Source data are provided as a Source Data file.

interesting phenomena: under the action of strain, VBM, conduction band minimum (CBM) and bandgap changed significantly along the y-axis (Supplementary Fig. 25, Supplementary Tables 2, 3)[51]. In particular, the band gap change of the MgO/MgF_2:Cr^{3+} heterojunction is significantly greater than that of MgF_2:Cr^{3+}. In the negative strain (compression) range, the bandgap of the heterojunction is significantly reduced, especially at -1% strain, where the bandgap change is the largest. In the positive strain (tensile) region, the bandgap also changes, further indicating that the MgO/MgF_2:Cr^{3+} heterojunction responds more significantly to strain (Fig. 6g). These results reveal the key role of strain in regulating the bandgap of materials and provide more possible pathways for the luminescence regulation of this heterojunction.

Finally, the change in carrier mobility may be a direct factor in improving ML performance. By calculating the carrier mobility of three-dimensional materials, the transfer characteristics of electrons can be obtained. The carrier mobility can be estimated using the deformation potential approximation under the electron-acoustic-phonon scattering mechanism. The mobility of 3D systems is[52]:

$$\mu_\beta^{3D} = \frac{e\langle\tau_\beta\rangle}{m^*} = \frac{2\sqrt{2\pi}e\,C_\beta^{3D}\left(\frac{\hbar}{2\pi}\right)^4}{3(k_B T)^{\frac{3}{2}} E_\beta^2 m^{*5/2}} \quad (4)$$

where m^* is the effective mass of the electron/hole, C_β^{3D} is the 3D elastic modulus, E_β is the deformation potential constant, T is the Kelvin temperature at room temperature (Supplementary Fig. 26). Among them, the slope of the linear fitting of CBM/VBM data under different strains is the value of deformation potential energy (Supplementary Fig. 27). Figure 6h shows the comparison of the mobility of electrons

and holes in $MgF_2:Cr^{3+}$ and $MgO/MgF_2:Cr^{3+}$. The electron mobility of the $MgO/MgF_2:Cr^{3+}$ heterostructure is $4.09 \times 10^2\ cm^2\ V^{-1}\ s^{-1}$, which is significantly higher than the electron mobility of $MgF_2:Cr^{3+}$ ($1.07 \times 10^2\ cm^2\ V^{-1}\ s^{-1}$), indicating that $MgO/MgF_2:Cr^{3+}$ has obvious advantages in electronic conduction performance. At the same time, there are also differences in hole mobility between the two materials. The hole mobility of $MgF_2:Cr^{3+}$ is $1.72 \times 10^2\ cm^2\ V^{-1}\ s^{-1}$, while that of $MgO/MgF_2:Cr^{3+}$ is $4.62 \times 10^2\ cm^2\ V^{-1}\ s^{-1}$, which is significantly higher than that of $MgF_2:Cr^{3+}$ (Supplementary Table 4). Overall, the $MgO/MgF_2:Cr^{3+}$ heterojunction exhibits strong conduction properties in both electron and hole mobility, especially in electron mobility. This huge difference in mobility may be the main factor in the improvement of ML performance, indicating that the heterojunction material has great application potential in optoelectronic device materials.

To further elucidate the influence of MgO incorporation on the ML performance of $MgF_2:Cr^{3+}$, it is essential to investigate the modulation of charge carrier behavior from the perspective of intrinsic defects. Therefore, first-principles calculations were performed to determine the formation energies of various typical intrinsic and complex defects in both $MgF_2:Cr^{3+}$ and $MgO/MgF_2:Cr^{3+}$ (Supplementary Fig. 28a). The results show that in the $MgF_2:Cr^{3+}$ system, fluorine vacancy ($V_F^{\cdot}$) and interstitial fluorine (i_F') defects have lower formation energies, especially the i_F' defect has the lowest formation energy, indicating that it is the easiest to form in the material. In contrast, the defect formation energy distribution changes significantly in the $MgO/MgF_2:Cr^{3+}$ heterostructure. The introduction of MgO induces local lattice strain and electronic structure reconstruction, which substantially lowers the formation energies of defects that are otherwise energetically unfavorable in the $MgF_2:Cr^{3+}$, such as i_F' and the $i_F' + V_F^{\cdot}$ defect complex. This shows that the presence of MgO not only promotes the stable generation of intrinsic defects, but also enhances the local enrichment ability and transmission efficiency of carriers in the interface region, thus providing favorable conditions for the generation of ML.

Based on the above results, the physical mechanism of self-powered NIR-ML in $MgO/MgF_2:Cr^{3+}$ heterostructures can be further revealed (Supplementary Fig. 28b). In $MgO/MgF_2:Cr^{3+}$, the heterojunction formed at the MgO/MgF_2 interface causes a band offset, providing an intrinsic driving force for charge carrier separation and migration. When the mechanical load is applied, the local stress-induced piezoelectric field further enhances the electric field intensity at the heterojunction, significantly strengthening the carrier generation and separation processes. Specifically, the piezoelectric field excites electrons in the trap state (D_0), causing them to be released and converted into free electrons (e^-) and holes (h^+). The free electrons are accelerated and injected into the CB, while the holes remain in the VB. The band tilting effects in both the conduction and valence bands further accelerate the migration of free electrons toward the heterojunction interface, while suppressing hole diffusion, thereby significantly enhancing the recombination efficiency of electrons and holes. The free electrons are then injected into the excited states of Cr^{3+} ions ($^4T_2$ and ^2E), and relax non-radiatively to lower excited states. Finally, the electrons return to the ground state ($^4A_2$) via radiative transitions, emitting NIR ML. In summary, MgO/MgF_2 heterostructures achieve efficient generation, migration and recombination of carriers under mechanical excitation conditions by regulating defect behavior and band structure, which constitutes the key mechanism of its excellent self-powered NIR-ML luminescence performance.

To evaluate the biocompatibility of $MgO/MgF_2:Cr^{3+}$ materials, especially their toxic effects on biological cells. The changes in cell viability of RAW264.7 cells after incubation with the material for 24, 48, and 72 h were detected by CCK-8 method and fluorescence microscopy (Supplementary Fig. 29). Figure 7a shows the changes in cell survival rate under treatment with different concentrations (0, 0.5, 1, 2.5, 5, 10, 20, 30, 40, 50, 60, 70, 80, 90, and 100 μg mL^{-1}). The horizontal axis represents the cell survival rate (%), and the vertical axis is the concentration of $MgO/MgF_2:Cr^{3+}$ (μg mL^{-1})[53]. The results show that the treatment of $MgO/MgF_2:Cr^{3+}$ materials has little effect on the survival rate of RAW264.7 cells, indicating that its toxicity is low. Although the cell survival rate decreased with increasing concentration, even at the highest concentration of 100 μg mL^{-1}, the cell survival rate remained at a high level (>90%), and no obvious large-scale cell death was observed.

In addition, three representative concentrations (1, 50, and 100 μg mL^{-1}) were selected for cell live-death staining observation at different time points (24, 48, and 72 h). All treatment groups showed strong green fluorescence, indicating that most cells are alive. Specially, even in the higher concentration treatment group, the cell population showed uniform green fluorescence, and no obvious red dead cell fluorescence was observed, further verifying that the material did not cause significant cell death at these concentrations (Fig. 7b, Supplementary Fig. 30). It should be noted that the cells also showed survival under other different microscope fields (Supplementary Fig. 31). The results showed that there was no significant decrease in cell viability at different concentrations and incubation times, indicating that all $MgO/MgF_2:Cr^{3+}$ have good biocompatibility and are suitable for further biomedical related research, especially in the fields of in vivo and in vitro biomechanical imaging.

Methods

Synthesis of $MgO/MgF_2:Cr^{3+}$ powders

A series of phosphors were synthesized by a high-temperature solid-state reaction method. According to the designed stoichiometric ratio, MgO (99.99%, Aladdin), MgF_2 (99.95%, Aladdin), and CrF_3 (99%, Macklin) were weighed as the initial raw materials. The weighed sample was poured into an agate bowl and ground for 20 min, transferred to a corundum crucible, and heated from room temperature to 1200 °C in a chamber furnace at a rate of 5 °C min^{-1} for 1 h. The samples were naturally cooled to room temperature and then poured into the agate bowl for complete grinding for further testing.

Fabrication of ML composites

Step 1: Wrap the ML powder with LDPE film and perform preliminary shaping using a thermoforming machine (AEQN8922, China). Step 2: Cut the LDPE film into 5 cm × 5 cm dimensions and secure it with a PET hard film. Step 3: Use a thermoforming machine to thermoform the secured PET film.

Preparation of piezoelectric devices

The ML powder sample was placed in a mold and pressed into a dense sheet (12 mm in diameter and 1.8 mm in thickness) using a tablet press at a pressure of 20 MPa, followed by polarization treatment for 20 min under a high-voltage DC electric field (2 kV). The copper foil electrodes were fixed on both sides of the pressed sample with conductive silver glue and the wires were led out, and then encapsulated with polyimide film. During the test, the wires were connected to the input end of the electrometer 6514, 2 N vertical pressure was applied, and the output current and voltage were recorded respectively.

Characterization

The crystallinity of all samples was confirmed by XRD using a Bruker D8 advance powder diffractometer with Cu Kα radiation (λ = 1.54059 Å) at room temperature. The raw XRD data were further analyzed using the Rietveld refinement method (GSAS software package) to confirm the formation of the target phase. The PL/PLE spectra, luminescence decay time, and PersL curves were recorded using the Edinburgh FLS980 fluorescence spectrometer equipped with a 450 W Xe lamp. XPS (Thermo SCIENTIFIC Nexsa) was equipped with a focused monochromatic Al K_α X-ray beam to examine the trap defects. For TL measurements, all samples were preirradiated for 2 min by a

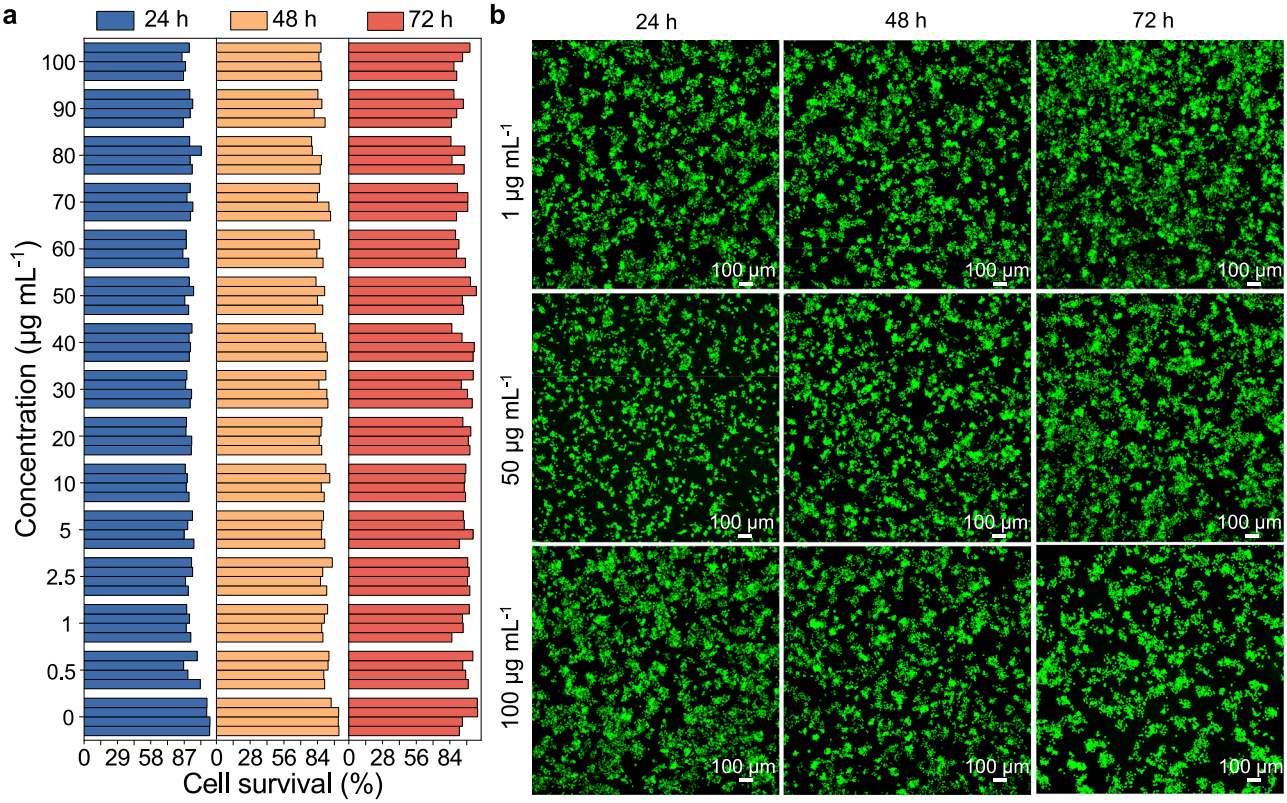

Fig. 7 | Biocompatibility assessment of MgO/MgF_2:Cr^{3+} in RAW264.7 macrophage cells. a Cell viability of RAW264.7 cells after incubation with MgO/MgF_2:Cr^{3+} dispersions at concentrations ranging from 0 to 100 μg mL^{-1} for 24, 48, and 72 h, as evaluated by a standard CCK-8 assay. All tested concentrations maintained high survival rates (>90%), indicating low cytotoxicity. Four cells were cultured simultaneously at each concentration (Supplementary Fig. 29). **b** Live/Dead fluorescence staining images of cells treated with 1, 50, and 100 μg mL^{-1} for 24, 48, and 72 h (Green, live cells; Red, dead cells in Supplementary Fig. 30). Predominant green fluorescence (viable cells) across all conditions further confirms excellent cytocompatibility. Scale bar: 100 μm. Raw image files for (**b**) are provided as Supplementary Data 1. Source data are provided as a Source Data file.

254 nm lamp at an output power of 30 W and an FJ427 A1 thermoluminescence dosimeter (CNNC, Beijing Nuclear Instruments Factory) in the range of 300–650 K. The surface morphology and corresponding mapping analyses were obtained from a SEM (Zeiss Sigma 500, Germany). The local work function or surface potential difference is tested using a KPFM using a Bruker Dimension icon/Dimension iconXR instrument. The current and voltage curves were recorded over time using an electrometer 6514. The current-voltage curves were recorded using Shanghai Chenhua CHI-660E. The tests of carrier mobility and carrier concentration were completed using the Hall effect test system, and the equipment used was the Accent HL5500 Hall System produced by Lake Shore, USA. The test conditions were as follows: the external magnetic field strength was 0.5 T, and the applied current range was −200 to 200 mA. UPS testing was performed using the ESCALAB 250Xi instrument produced by Thermo Scientific to characterize the electronic energy state structure and work function of the material. The ML spectra were recorded by a universal press machine (CMT1104, China), a photocounting system (QE650pro, Ocean Optics), and a computer.

Cell counting kit-8 (CCK-8) assay

RAW264.7 cells were cultured in a 5% CO_2, 37 °C incubator. RAW264.7 cells in the logarithmic growth phase were taken, the cell count was performed, the cell concentration was adjusted, and 5000 cells per well were inoculated into a 96-well plate, and cultured overnight in a 5% CO_2, 37 °C incubator. According to the grouping, 100 μL per well of the sample prepared with complete medium was added to each well, and 4 replicates were made for each treatment group, and the culture was continued for 24 h. The culture medium was removed, and 10 μL CCK8 detection solution was added at 100 μL, and cultured in a 5% CO_2, 37 °C incubator for 4 h. The absorbance value at 490 nm was detected by an enzyme reader. The absorbance values of each group were entered into Excel and the relative activity was calculated (relative activity = (OD value of the experimental group - background OD value)/(mean OD value of the control group - background OD value)). Among them, the background OD value of the experimental group is the absorbance of the material and culture medium, and the background OD value of the control group is the absorbance of the culture medium and CCK8.

Cell live-dead staining method

(1) RAW264.7 cells were cultured in a 5% CO_2, 37 °C constant temperature incubator. (2) L929 cells in the logarithmic growth phase were taken, the cell count was performed, the cell concentration was adjusted, and 50,000 cells per well were inoculated into a 12-well plate, and cultured in a 5% CO_2, 37 °C constant temperature incubator overnight. According to the above grouping treatment, the culture was continued for 24 h. (3) Calcein AM (1000X) and PI (1000X) were diluted 1000 times with PBS and set aside. (4) 1 mL of Calcein AM/PI detection working solution was added and incubated at 37 °C in the dark for 30 min. (5) After the incubation, the staining effect was observed under a fluorescence microscope (Calcein AM is green fluorescence, $\lambda_{ex}/\lambda_{em}$ = 494/517 m; PI is red fluorescence, $\lambda_{ex}/\lambda_{em}$ = 535/617 m).

Calculation

All the structural and electronic properties involved in this paper were calculated by VASP software[54,55]. The interaction between the ionic reality and the electrons was described using the projector-augmented

wave (PAW)[56]. The electronic exchange and correlation energies were described using the GGA-PBE functional[57]. The plane-wave cutoff energy was set to 400 eV, with the conjugate gradient method employed for atomic position optimization. The convergence criteria for total energy and atomic forces were set to 1×10^{-4} eV and 0.05 eV $Å^{-1}$, respectively. Spin polarization and van der Waals interactions (DFT-D3) were also accounted for in the calculations[58]. We used the MgF_2 crystal [101] plane of $P4_2/mnm$ space group and the MgO crystal [110] plane of Fm-3m to construct the heterojunction. A 20 Å vacuum layer was introduced along the c-axis to prevent interlayer interactions. Brillouin zone sampling was performed using the Γ-centered Monkhorst-Pack scheme[59]. Structural relaxation and electronic property calculations employed k-point grids of $1 \times 1 \times 1$ and $2 \times 6 \times 4$, respectively.

Reporting summary

Further information on research design is available in the Nature Portfolio Reporting Summary linked to this article.

Data availability

The data that support the findings of this study are available from the corresponding author upon request. Raw image files for Fig. 7b and Supplementary Fig. 31 are provided as Supplementary Data 1. Source data are provided with this paper.

References

1. Xie, Z. et al. Isostructural doping for organic persistent mechanoluminescence. *Nat. Commun.* **15**, 3668 (2024).
2. Shao, P. et al. Tunable and enhanced mechanoluminescence in $LiYGeO_4$:Tb^{3+} via $Bi^{3+} \rightarrow Tb^{3+}$ energy transfer. *J. Mater. Chem. C* **11**, 2120–2128 (2023).
3. Wu, S. et al. Regulating broadband near-infrared mechanoluminescence via energy-level engineering for potential biomechanical imaging. *Laser Photonics Rev.* **19**, 2401441 (2025).
4. Xiao, B. et al. Multicolor mechanoluminescence in $Sr_2Ga_2GeO_7$: Pr^{3+} for stress sensing and anticounterfeiting. *Adv. Opt. Mater.* **11**, 2300911 (2023).
5. Xiao, Y. et al. Cation-defect-induced self-reduction towards efficient mechanoluminescence in Mn^{2+}-activated perovskites. *Mater. Horiz.* **10**, 3476–3487 (2023).
6. Hou, B. et al. An interactive mouthguard based on mechanoluminescence-powered optical fibre sensors for bite-controlled device operation. *Nat. Electron* **5**, 682–693 (2022).
7. Suo, H. et al. A broadband near-infrared nanoemitter powered by mechanical action. *Matter* **6**, 2935–2949 (2023).
8. Wu, Y., Wu, S., Xiong, P. & Wang, S. Near-infrared mechanoluminescence from $Sr_3Sn_2O_7$:Nd^{3+} for potential bioimaging and non-destructive detection. *J. Rare Earths*, https://doi.org/10.1016/j.jre.2025.1001.1008 (2025).
9. Wu, S. et al. Multiple defect-induced high-resolution near-infrared mechanoluminescent materials for non-destructive detection of blood glucose and lipids. *Adv. Mater.* **36**, 2408508 (2024).
10. Shao, P. et al. Near-infrared mechanoluminescence from Cr^{3+}-doped spinel nanoparticles for potential oral diseases detection. *Small* **20**, 2402352 (2024).
11. Li, C. et al. Highly robust and soft biohybrid mechanoluminescence for optical signaling and illumination. *Nat. Commun.* **13**, 3914 (2022).
12. Xiong, P. & Peng, M. Near infrared mechanoluminescence from the Nd^{3+} doped perovskite $LiNbO_3$:Nd^{3+} for stress sensors. *J. Mater. Chem. C* **7**, 6301–6307 (2019).
13. Xiong, P., Peng, M., Cao, J. & Li, X. Near infrared mechanoluminescence from $Sr_3Sn_2O_7$: Nd^{3+} for in situ biomechanical sensor and dynamic pressure mapping. *J. Am. Ceram. Soc.* **102**, 5899–5909 (2019).
14. Zhang, Y. et al. Remote regulation of optogenetic proteins by a magneto-luminescence microdevice. *Adv. Funct. Mater.* **31**, 2006357 (2021).
15. Wang, H. et al. Oscillatory mechanoluminescence of Mn^{2+}-doped SrZnOS in dynamic response to rapid compression. *Nat. Commun.* **16**, 548 (2025).
16. Katsumata, T., Komuro, S. & Aizawa, H. Fracto-mechanoluminescence from ruby and Cr doped spinel in cutting, grinding and polishing processes. *J. Lumin* **154**, 511–514 (2014).
17. Xiong, P. et al. Self-recoverable mechanically induced instant luminescence from Cr^{3+}-doped $LiGa_5O_8$. *Adv. Funct. Mater.* **31**, 2010685 (2021).
18. Dou, C. et al. Self-recoverable and NIR-I to NIR-II tunable broadband mechanoluminescence of Cr^{3+}-doped antimonate double perovskites. *Adv. Funct. Mater.* **35**, 2419716 (2025).
19. Liu, S. et al. Near-infrared mechanoluminescence of Cr^{3+} doped gallate spinel and magnetoplumbite smart materials. *Adv. Funct. Mater.* **33**, 2209275 (2023).
20. Liu, Z. et al. NIR mechanoluminescence from Cr^{3+} activated $Y_3Al_5O_{12}$ with intense zero phonon line. *Adv. Funct. Mater.* **33**, 2214497 (2023).
21. Wang, Y. et al. Multi-mode luminescence in smart near-infrared Cr^{3+}/Pr^{3+} codoped $SrGa_{12}O_{19}$ phosphors induced by three distinct excitation mechanisms. *ACS Appl. Mater. Interfaces* **16**, 33855–33864 (2024).
22. Wang, Y. et al. Simultaneous NIR photoluminescence and mechanoluminescence from Cr^{3+} activated $MgGa_2O_4$ phosphors with multifunctions for optical sensing. *J. Mater. Chem. C***12**, 3654–3661 (2024).
23. Yu, S. et al. Self-recoverable and cyclically stable near-infrared mechanoluminescence for dual-mode mechanics visualization and biomechanics detection. *Chem. Eng. J.* **474**, 145542 (2023).
24. Yu, X. et al. Intense NIR mechanoluminescence from Al^{3+}-regulated $MgGa_2O_4$: Cr^{3+}. *Chem. Eng. J.* **491**, 152155 (2024).
25. Bu, W. et al. Near-infrared mechanoluminescence of $Gd_3Ga_5O_{12}$: Cr^{3+}, La^{3+} for biological stress imaging. *Laser Photonics Rev.* **19**, 2400893 (2024).
26. Xiao, B. et al. Broadband near-infrared mechanoluminescence in Cr^{3+} doped $Mg_3Ga_2GeO_8$. *Chem. Eng. J.* **498**, 155040 (2024).
27. Wu, S. et al. Cr^{3+}-activated broadband near-infrared mechanoluminescence in garnet compound. *Nano Energy* **116**, 108811 (2023).
28. Wu, S. et al. Realizing near infrared mechanoluminescence switch in LAGO: Cr based on oxygen vacancy. *Small* **20**, 2309034 (2024).
29. Shao, P. et al. Self-recoverable NIR mechanoluminescence from Cr^{3+} doped perovskite type aluminate. *Adv. Powder Mater.* **3**, 100165 (2024).
30. Deng, Y. et al. Enhancing the mechanoluminescence of traditional ZnS: Mn phosphors via Li^+ Co-doping. *J. Lumin.* **225**, 117364 (2020).
31. Xia, M. et al. Kinetic Wulff-shaped heteroepitaxy of phase-pure 2D perovskite heterostructures with deterministic slab thickness. *Nat. Synth.* **4**, 380–390 (2025).
32. Li, X. et al. Proximity-induced chiral quantum light generation in strain-engineered $WSe_2/NiPS_3$ heterostructures. *Nat. Mater.* **22**, 1311–1316 (2023).
33. Niu, R. et al. Ferroelectricity with concomitant Coulomb screening in van der Waals heterostructures. *Nat. Nanotechnol.* **20**, 346–352 (2025).
34. Zheng, T. et al. Mechanoluminescence and photoluminescence heterojunction for superior multimode sensing platform of friction, force, pressure, and temperature in fibers and 3D-printed polymers. *Adv. Mater.* **35**, 2304140 (2023).
35. Ning, J. et al. MgF_2:Mn^{2+}: novel material with mechanically-induced luminescence. *Sci. Bull.* **67**, 707–715 (2022).

36. Cai, C. et al. All-lanthanide mechanoluminescence from transparent Ln-doped MgF_2@Elastomer for flexible and stretchable lighting and stress sensing. *Adv. Mater. Technol.* **9**, 2301855 (2024).
37. Rajendran, V. et al. Chromium cluster luminescence: advancing near-infrared light-emitting diode design for next-generation broadband compact light sources. *Adv. Opt. Mater.* **12**, 2302645 (2024).
38. Liu, G. et al. $MgAl_2O_4$:Cr^{3+} translucent ceramics with tunable broadband near-infrared luminescence for laser-driven light source detection. *InfoMat.* **7**, e70020 (2025).
39. Chen, G. et al. Unlocking Cr^{3+}-Cr^{3+} coupling in spinel: ultrabroadband near-infrared emission beyond 900 nm with high efficiency and thermal stability. *ACS Appl Mater. Interfaces* **16**, 30185–30195 (2024).
40. Yu, S. et al. Modulation of sharp-line red emissions to efficient broadband near-infrared luminescence in Cr^{3+}-activated spinel phosphors via defect engineering. *Adv. Opt. Mater.* **13**, 2403507 (2025).
41. Tao, J. et al. Self-powered tactile sensor array systems based on the triboelectric effect. *Adv. Funct. Mater.* **29**, 1806379 (2019).
42. Bai, Y. et al. Interfacial triboelectrification-modulated self-recoverable and thermally stable mechanoluminescence in mixed-anion compounds. *Nano Energy* **96**, 107075 (2022).
43. Wang, W., Wang, S., Gu, Y., Zhou, J. & Zhang, J. Contact-separation-induced self-recoverable mechanoluminescence of CaF_2:Tb^{3+}/PDMS elastomer. *Nat. Commun.* **15**, 2014 (2024).
44. Chen, C. et al. A method for quantitatively separating the piezoelectric component from the as-received "Piezoelectric" signal. *Nat. Commun.* **13**, 1391 (2022).
45. Wang, W. et al. Self-powered and self-recoverable multimodal force sensors based on trap state and interfacial electron transfer. *Angew. Chem., Int. Ed.* **63**, e202404060 (2024).
46. Zheng, P. et al. Flexible optical fiber stress/temperature dual-mode sensing based on CaZnOS:Nd,Er. *Adv. Funct. Mater.* https://doi.org/10.1002/adfm.202505094 (2025).
47. Liu, S. et al. Near-infrared mechanoluminescence of Cr^{3+} doped gallate spinel and magnetoplumbite smart materials. *Adv. Funct. Mater.* **33**, 2209275 (2022).
48. Dange, K., Yogi, R. & Shukla, A. Two-dimensional transition-metal dichalcogenide-based bilayer heterojunctions for efficient solar cells and photocatalytic applications. *Phys. Rev. Appl.* **23**, 014008 (2025).
49. Peng, D. et al. A ZnS/CaZnOS heterojunction for efficient mechanical-to-optical energy conversion by conduction band offset. *Adv. Mater.* **32**, 1907747 (2020).
50. Wang, C. et al. Interface-mediated mechanoluminescence enhancement from heterojunction phosphors: experiment and theory. *ACS Appl Mater. Interfaces* **15**, 30891–30901 (2023).
51. Shao, Z., Zhou, G., Wang, C. & Yang, L. A new carbon allotrope with high carrier mobility and optical absorption. *Phys. Chem. Chem. Phys.* **27**, 782–790 (2025).
52. Xi, J., Long, M., Tang, L., Wang, D. & Shuai, Z. First-principles prediction of charge mobility in carbon and organic nanomaterials. *Nanoscale* **4**, 4348–4369 (2012).
53. Shen, L. et al. NIR-II imaging for tracking the spatiotemporal immune microenvironment in atherosclerotic plaques. *ACS Nano* **18**, 34171–34185 (2024).
54. Kresse, G. & Furthmüller, J. Efficient iterative schemes for ab initio total-energy calculations using a plane-wave basis set. *Phys. Rev. B* **54**, 11169–11186 (1996).
55. Kresse, G. & Furthmüller, J. Efficiency of ab-initio total energy calculations for metals and semiconductors using a plane-wave basis set. *Comput. Mater. Sci.* **6**, 15–50 (1996).
56. Kresse, G. & Joubert, D. From ultrasoft pseudopotentials to the projector augmented-wave method. *Phys. Rev. B* **59**, 1758–1775 (1999).
57. Perdew, J. P., Burke, K. & Ernzerhof, M. Generalized gradient approximation made simple. *Phys. Rev. Lett.* **77**, 3865–3868 (1996).
58. Grimme, S., Antony, J., Ehrlich, S. & Krieg, H. A consistent and accurate ab initio parametrization of density functional dispersion correction (DFT-D) for the 94 elements H-Pu. *J. Chem. Phys.* **132**, 154104 (2010).
59. Monkhorst, H. J. & Pack, J. D. Special points for Brillouin-zone integrations. *Phys. Rev. B* **13**, 5188–5192 (1976).
60. Li, X. et al. Smart semiconductor-heterojunctions mechanoluminescence for printable and wearable sports light sources. *Mater. Des.* **225**, 111589 (2023).
61. Yue, Y. et al. Smart films based on semiconductor heterojunctions of mechanoluminescent sulfide and sulfur oxide for stress sensing and anti-counterfeiting applications. *Chem. Eng. J.* **495**, 153141 (2024).
62. Li, L. et al. Stress-triggered mechanoluminescence in ZnO-based heterojunction for flexible and stretchable mechano-optics. *Adv. Funct. Mater.* **33**, 2301372 (2023).
63. Jia, J. et al. Ternary-host and heterojunction enabled eye-visible elastic mechanoluminescence from $(Ca_{0.5}Sr_{0.5})$ZnOS/xZnS/Mn^{2+}. *J. Phys. Chem. C* **126**, 1523–1530 (2022).
64. Li, W. et al. Theoretical understanding of defects-driven mechanoluminescence for Pr^{3+}-doped $NaNbO_3$/$LiNbO_3$ heterojunctions. *J. Rare Earths.* **43**, 691-700 (2025)

Acknowledgements

The authors gratefully acknowledge the support from the National Natural Science Foundation of China (No. 52202003, 52072132), Guangdong Basic and Applied Basic Research Foundation (No. 2023A1515011893, c21140500002457). Sincerely, P.X.X. expresses special thanks to Prof. Dr. M.Y. Peng for his rigorous guidance in research studies.

Author contributions

Conceptualization: S. Wu and P.X. Xiong; Data Curation: S. Wu, S.Y. Wang; Writing—Original Draft: S. Wu and P.X. Xiong; Visualization: Y.Z. Wang and P.X. Xiong; Supervision: Z.G. Shao, Y.Z. Wang and P.X. Xiong.

Competing interests

The authors declare no competing interests.

Additional information

Supplementary information The online version contains supplementary material available at https://doi.org/10.1038/s41467-025-63980-4.

Correspondence and requests for materials should be addressed to Puxian Xiong.

Peer review information *Nature Communications* thanks Haider Golam and the other anonymous reviewer(s) for their contribution to the peer review of this work. A peer review file is available.